




Manipulating generalized Dirac cones in subwavelength dipolar arraysMaría Blanco de Paz ^{1,2}, Alejandro González-Tudela ³, and Paloma A. Huidobro ^{2,*}¹*Donostia International Physics Center, 20018 Donostia-San Sebastián, Spain*²*Instituto de Telecomunicações, Instituto Superior Técnico, University of Lisbon, Avenida Rovisco Pais 1, 1049-001 Lisboa, Portugal*³*Institute of Fundamental Physics, CSIC, Calle Serrano 113b, 28006 Madrid, Spain*

(Received 24 March 2022; accepted 29 August 2022; published 12 September 2022)

We discuss the emergence and manipulation of generalized Dirac cones in the subradiant collective modes of a subwavelength dipolar array. We consider a collection of single quantum emitters modeled as point dipoles arranged in a honeycomb lattice with subwavelength periodicity. While conventional honeycomb arrays host bound modes that display Dirac cones at the K and K' points, we show that introducing uniaxial anisotropy in the lattice results in modified dispersion relations. These include the tilting of Dirac cones arising purely due to long-range, retarded, electromagnetic coupling in the lattice, which changes the local density of states at the Dirac point from vanishing (type I) to diverging (types II and III), the emergence of semi-Dirac points, with linear and quadratic dispersions in orthogonal directions, and the anisotropic movement of Dirac cones away from the K and K' points. Such energy dispersions can modify substantially the dynamics of local probes, such as quantum emitters, for which they have been shown to induce anisotropic power-law interactions.

DOI: [10.1103/PhysRevA.106.033505](https://doi.org/10.1103/PhysRevA.106.033505)**I. INTRODUCTION**

Metasurfaces enable the tuning of light-matter interactions by exploiting collections of subwavelength nanoantennas made of metallic or dielectric nanostructures, even realizing properties that are not available in natural materials [1–3]. Conventionally, metasurfaces have been designed as periodic arrays of nanoresonators such as dielectric or plasmonic nanoantennas. These setups have successfully led to multiple applications, including sensing [4] and nanoscale lasing [5], as well as topological protection [6–10], polaritonic edge states [11], and even gauge fields in subwavelength arrays [12].

Recently, the possibility of realizing quantum metasurfaces has been considered [13–15]. In their most fundamental realization, these make use of single-photon emitters such as atomic transitions as the most elementary subwavelength antennas [16], which operate at the single-photon level and with very low radiative loss [17].

By arranging single-photon emitters in lattices of subwavelength periodicities, coherent dipole-dipole interactions between all the quantum emitters in the lattice result in cooperative effects that lead to drastic changes in the optical properties of the emitters when they are placed in the array [13,18–23]. An important instance of cooperative effects is the subradiant optical states whose coupling to the photonic environment is greatly reduced. Subradiant modes can be harnessed for selectively improving radiation in a given desired channel [24], for mediating nontrivial emitter-emitter interactions when additional atoms are placed nearby [25–29], generating topological edge modes [30,31] or creating magnetic responses at optical frequencies [32,33]. These exciting

perspectives have triggered experimental interest in the topic, and have already crystallized in the first experimental realization of a subradiant optical mirror [34]. Among the prospects of quantum metasurfaces for controlling the interaction between photons and optical media is the generation of nontrivial photonic energy dispersions, akin to those one can obtain with photonic crystals [35], which lead to extreme and exotic forms light-matter interactions and their exploitation as quantum photonic setups [25–29].

On the other hand, since the discovery of the remarkable electronic properties of graphene and how these emerge from isotropic linear energy dispersions [36], the realization of synthetic Dirac dispersions has attracted much attention in photonics, as a variety of photonic platforms enable the possibility of synthesizing and even manipulating a plethora of unconventional energy dispersions [37–47]. Conventional Dirac cones, such as the ones found in graphene, present an isotropic and linear energy dispersion and are extremely robust against perturbations of the lattice. The reason for this is that they have a topological origin: In the presence of time-reversal and inversion symmetry, they appear in pairs of opposite topological charge and can only disappear by merging with a cone of the opposite charge [48–50]. On the other hand, generalized Dirac dispersions are possible. Figure 1 schematically shows the conventional dispersions in Dirac media [Fig. 1(a)], as well as the new generalized dispersions enabled by anisotropy. First, Dirac cones can be tilted [Fig. 1(b)] such that the isofrequency contours at the degeneracy are either still a point (type I, depicted left), a line (critical, or type III, middle) or two lines (type II, right) [51]. This involves remarkable changes in the density of states, which changes from zero to infinity. On the other hand, anisotropic cones where the dispersion is linear in one direction but becomes quadratic in the orthogonal one are

*p.arroyo-huidobro@lx.it.pt

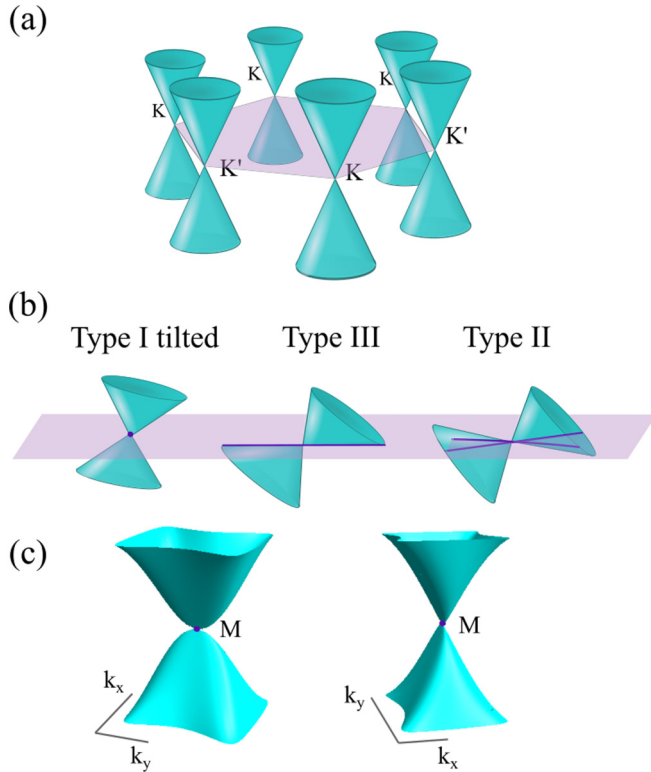


FIG. 1. Dirac and generalized Dirac dispersions. (a) Sketch of the Dirac cones of the conventional honeycomb lattice distributed in the Brillouin zone. Introducing anisotropy in the lattice allows one to manipulate the crossings and generate (b) tilted cones of types I (left), II (right), and III or critical (middle), as well as (c) semi-Dirac cones, which present linear and quadratic dispersions in orthogonal directions in reciprocal space.

also possible, as sketched in Fig. 1(c), and named semi-Dirac cones [52,53].

These unconventional structured photonic baths have the potential to greatly modify the quantum dynamics of probe emitters placed in the vicinity of the metasurface. Dirac cones have already been shown to lead to exotic quantum dynamics and long-range photon-mediated interactions [54–57]. A quantum emitter tuned to a Dirac point displays an unconventional (nonexponential) decay despite the vanishing density of states, which is attributed to a power-law photonic mode localized around the emitter. This so-called quasibound state can mediate long-range interactions between quantum emitters, which can also be made anisotropic by employing generalized Dirac dispersions [58].

In this work we discuss how generalized Dirac dispersions emerge and can be manipulated in subwavelength dipolar arrays. We do so by introducing uniaxial anisotropy in a subwavelength honeycomb lattice of point dipoles, which model quantum emitters as dipolar two-level systems. The lattice anisotropy enables the emergence of semi-Dirac and tilted Dirac cones. In a previous work [58], we showed how anisotropic tight-binding lattices provide a platform to interface unconventional Dirac dispersions and probe quantum emitters for a specific geometry. Here we consider more general subwavelength arrays of emitters interacting through

full long-range dipole-dipole interactions, as is the case with possible experimental scenarios such as arrays of cold atoms where long-range retarded interactions are unavoidable. This way we determine the parameter range where such unconventional dispersions emerge and we also identify how tilted Dirac cones emerge purely due to retarded electromagnetic coupling between the dipoles. Therefore, by studying unconventional Dirac dispersion in radiatively coupled lattices, we go beyond previous work based on tight-binding models [45–51,58].

The paper is structured as follows. We start by outlining the theoretical framework that allows us to calculate the dispersion relations in these subwavelength lattices with long-range interactions. After revisiting the properties of Dirac cones in honeycomb lattices, we first consider the out-of-plane modes of anisotropic honeycomb lattices and demonstrate the emergence of semi-Dirac cones and the anisotropic displacement of Dirac cones in reciprocal space. Next we consider the in-plane modes where we find another instance of semi-Dirac cones, as well as tilted Dirac cones and anisotropic displacements of Dirac cones. Finally, we present a more detailed discussion on the effect of retardation in these generalized dispersions.

II. ANISOTROPIC LATTICES AND THEORETICAL FRAMEWORK

We consider a generalized version of the honeycomb lattice that allows us to realize anisotropic arrays. As depicted in Fig. 2, these are non-Bravais lattices with two atoms per unit cell, described by primitive vectors $\mathbf{a}_{1/2} = d_0\sqrt{3}/2(\sqrt{3}\hat{\mathbf{e}}_x \pm \hat{\mathbf{e}}_y)$, with d_0 the nearest-neighbor distance of the honeycomb lattice [Fig. 2(a)] and with basis vector $\mathbf{d} = -d_{\text{intra}}\hat{\mathbf{e}}_x$. Here d_{intra} and correspondingly d_{inter} represent the intracell and intercell nearest-neighbor distances. In order to realize anisotropic lattices, we allow these two distances to be different $d_{\text{intra}} \neq d_{\text{inter}}$ and their ratio defines the anisotropy parameter $\beta = d_{\text{intra}}/d_{\text{inter}}$ ¹.

For a standard honeycomb lattice, $d_{\text{intra}} = d_{\text{inter}} = d_0$ such that the distance between nearest neighbors is the same in all directions and $\beta = 1$. On the other hand, $\beta < 1$ represents an anisotropic lattice where the two dipoles in the unit cell are pushed together [see Fig. 2(b)], which creates an imbalance in the nearest-neighbor distance in different directions, $d_{\text{intra}} \neq d_{\text{inter}}$. Similarly, for $\beta > 1$ the two atoms in the unit cell are pushed apart. The unbalanced nearest-neighbor distance affects the interactions between all elements in the lattice and results in a variety of generalized Dirac cones, as we discuss in detail in the following. Finally, while d_0 is the nearest-neighbor distance only in the honeycomb case, we will use it to characterize the periodicity of all the lattices since it defines the size of the lattice vectors as $|\mathbf{a}_{1/2}| = 2\sqrt{3}d_0$.

¹We note that the maximum value β can take is $\beta_{\text{max}} = 1.7321$. For this value of β , the anisotropy is maximum, corresponding to a rectangular lattice, and values of $\beta > \beta_{\text{max}}$ can be mapped to $\beta < \beta_{\text{max}}$. On the other hand, we keep $\beta \gtrsim 0.5$ to avoid unphysically close distances between the dipoles.

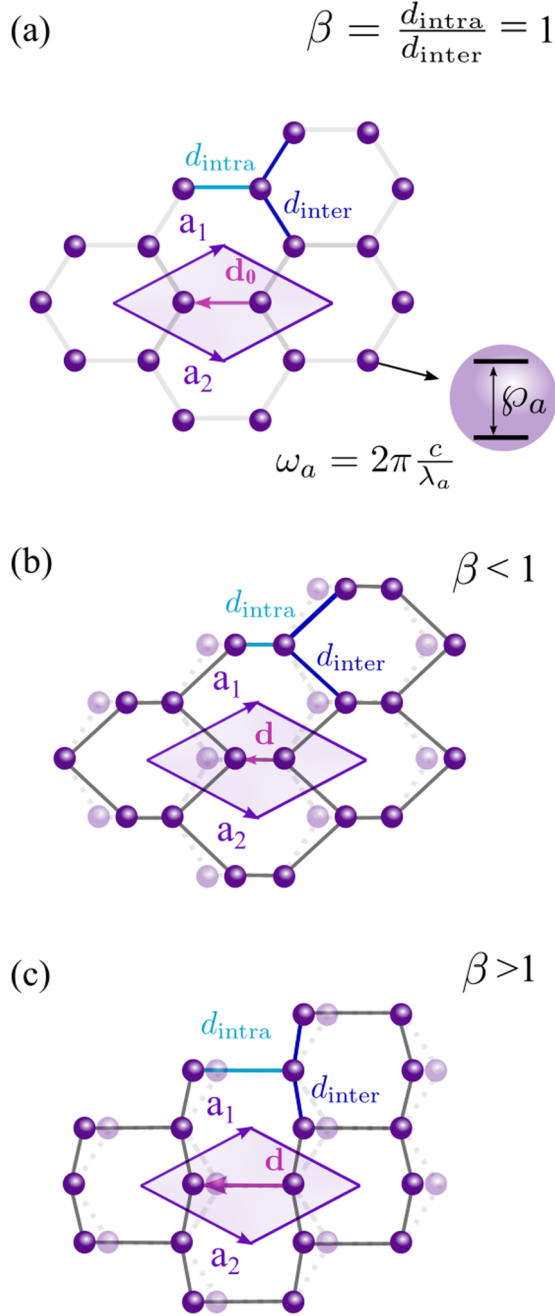


FIG. 2. Geometry of the quantum metasurfaces: a periodic array of single quantum emitters arranged in a non-Bravais lattice with two sites per unit cell. Starting from (a) a honeycomb lattice, anisotropic lattices are generated by pushing (b) together or (c) apart, in the horizontal direction, the two emitters contained in the unit cell. In all cases the basis vectors $\mathbf{a}_{1/2}$ and the unit cell are kept the same; what varies is the ratio between the intra- and intercell nearest-neighbor distances d_{intra} and d_{inter} , respectively, which characterizes the degree of anisotropy through the parameter $\beta = d_{\text{intra}}/d_{\text{inter}}$.

Each lattice site in the two-dimensional array contains a single emitter that we model as a two-level system with resonance frequency ω_a and polarization dipole $\hat{\rho}_a$. The dynamics of the emitters array can be described through an effective

non-Hermitian Hamiltonian [24,59]

$$\frac{H}{\hbar} = \sum_{j=1}^{N_A} \left(\omega_a - i \frac{\Gamma_a}{2} \right) \sigma_{ee}^j + \sum_{\substack{j=1 \\ i \neq j}}^{N_A} \left(J_{ij} - i \frac{\Gamma_{ij}}{2} \right) \sigma_{eg}^i \sigma_{ge}^j, \quad (1)$$

where j is a index running over all emitters in the metasurface (N_A), placed at positions \mathbf{r}_j , and $\Gamma_a = |\hat{\rho}_a|^2 \omega_a^3 / 3\pi \hbar c^3$ is the individual free-space decay rate. The coherent (J_{ij}) and incoherent (Γ_{ij}) photon-mediated interactions among emitters are given by the free-space Green's dyadic $\mathbf{G}_0(\mathbf{r}_i - \mathbf{r}_j)$ [60,61],

$$J_{ij} = -\frac{3\pi \Gamma_a c}{\omega_a} \text{Re}[\hat{\rho}_i^* \cdot \mathbf{G}_0(\mathbf{r}_i - \mathbf{r}_j) \cdot \hat{\rho}_j], \quad (2)$$

$$\frac{\Gamma_{ij}}{2} = \frac{3\pi \Gamma_a c}{\omega_a} \text{Im}[\hat{\rho}_i^* \cdot \mathbf{G}_0(\mathbf{r}_i - \mathbf{r}_j) \cdot \hat{\rho}_j], \quad (3)$$

where $\hat{\rho}_i = \rho_i / |\rho_i|$,

$$\mathbf{G}_0(\mathbf{r}) = \frac{1}{4\pi} \left[\mathbb{1} + \frac{\nabla \otimes \nabla}{k_0^2} \right] \frac{e^{ik_0|\mathbf{r}|}}{|\mathbf{r}|}, \quad (4)$$

and $k_0 = \omega/c$. Thus, the above Hamiltonian contains the individual free-space decays but also long-range retarded interactions between all the emitters in the lattice. Importantly, the dipole-dipole interactions described by the Green's function are long range, with terms that decay as $1/r^3$, $1/r^2$, and $1/r$. Additionally, interactions involve all the elements in the lattice and depend on the polarization of the electromagnetic fields. The geometry of the array generates two sets of modes: in-plane modes where the dipole's polarization is contained in the plane of the array and out-of-plane modes with dipoles polarized orthogonal to the lattice plane.

The eigenstates of the emitter array described by the above Hamiltonian can be found in the single-excitation subspace by looking for Bloch modes,

$$S_{\mathbf{k}}^\dagger = \frac{1}{\sqrt{N}} \sum_{n=1}^N \sum_{m=1}^2 \sigma_{eg}^{n,m} e^{i\mathbf{k} \cdot \mathbf{r}_n}, \quad (5)$$

where $\mathbf{k} = (k_x, k_y)$ is the mode wave vector in the plane of the array and we take into account that we have a non-Bravais lattice, with the sums now running over n , up to the total number of unit cells (N) and over the two sites per unit cell (m). Obtaining the eigenenergies of the Bloch modes from the above Hamiltonian then reduces to diagonalizing the matrix [59]

$$\begin{aligned} \mathbf{M}_{\mathbf{k}}^{\alpha\beta, \mu\nu} = & \left(\omega_a - i \frac{\Gamma_a}{2} \right) \delta_{\alpha\beta} \delta_{\mu\nu} \\ & - \frac{3\pi \Gamma_a c}{\omega_a} \left[\sum_{m=1}^2 \sum_{\mathbf{R}_n \neq 0} e^{-i\mathbf{k} \cdot \mathbf{R}_n} G_0^{\alpha\beta}(\mathbf{R}_n) \delta_{m\mu} \delta_{m\nu} \right. \\ & + \sum_{\mathbf{R}_n} e^{-i\mathbf{k} \cdot \mathbf{R}_n} G_0^{\alpha\beta}(\mathbf{R}_n + \mathbf{d}) \delta_{1\mu} \delta_{2\nu} \\ & \left. + \sum_{\mathbf{R}_n} e^{-i\mathbf{k} \cdot \mathbf{R}_n} G_0^{\alpha\beta}(\mathbf{R}_n - \mathbf{d}) \delta_{2\mu} \delta_{1\nu} \right], \quad (6) \end{aligned}$$

where $\{\mathbf{R}_n\}$ represent the in-plane position vectors of all the unit cells in the lattice. Index n runs from 0 to N , $\{\alpha, \beta\}$ run over the three spatial degrees of freedom, and $\{\mu, \nu\}$

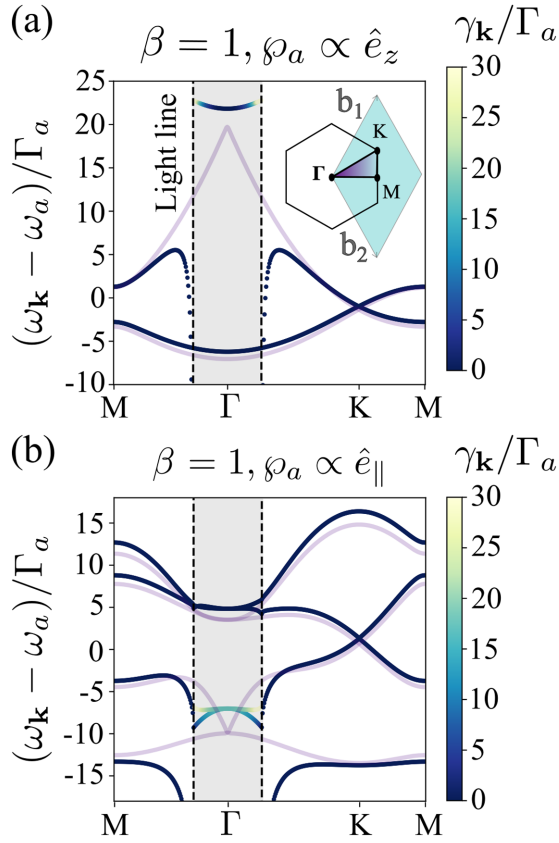


FIG. 3. Photonic band structure of honeycomb emitter arrays: dispersion relations of (a) out-of-plane and (b) in-plane modes for a honeycomb lattice of single quantum emitters with resonance frequency ω_a and individual decay rate Γ_a . Dirac crossings are visible at the K or K' points for both sets of modes. The decay rate of the modes is color coded, with the scale bar given in (b). Results from a quasistatic approximation are plotted as a light purple line. The region within the light cone is shaded in gray. The periodicity of the lattice is determined by the nearest-neighbor distance $d_0 = 0.1\lambda_a$. The relevant parameters are $\lambda_a = 790$ nm and $\Gamma_a = 2\pi \times 6$ MHz.

run over the two lattice sites. Hence $\mathbf{M}_{\mathbf{k}}$ is a 6×6 matrix with eigenvalues $\omega_{\mathbf{k}} - i\frac{\gamma_{\mathbf{k}}}{2}$, which represent the photonic band structure ($\omega_{\mathbf{k}}$) and the radiative decay of the Bloch modes ($\gamma_{\mathbf{k}}$). The lattice sums of the Green's tensor that appear in Eq. (6) are slowly convergent due to the long-range interactions and we employ the Ewald method to perform them efficiently [62,63]. We remark that solving the Hamiltonian in the single-excitation subspace is equivalent to a classical coupled-dipole approach [10]. While a classical calculation is enough for the purposes of this paper, the above formalism constitutes the basis of calculations beyond a single excitation [58].

III. DIRAC CONES IN A HONEYCOMB SUBWAVELENGTH DIPOLAR ARRAY

We first apply the theoretical formalism to revisit the case of a honeycomb emitter array [31,59]. Figure 3 presents the photonic band structure for the two out-of-plane modes $\hat{\rho}_i \propto \hat{e}_z$ [Fig. 3(a)] and the four in-plane modes $\hat{\rho}_i \propto \hat{e}_{\parallel}$ [Fig. 3(b)] of the honeycomb lattice $\beta = 1$. The array periodicity is given by the chosen nearest-neighbor distance $d_0 = 0.1\lambda_a$, with

$\lambda_a = 2\pi c/\omega_a$, here and throughout this work unless stated otherwise. This distance determines the position of the light line, which separates radiative and nonradiative modes. In the region within the light line, shaded in gray, modes have a nonzero radiative width, which is color coded in the plot [scale bar in Fig. 3(b)]. As seen in the figure, the most radiative modes present strong interactions with the light line and beyond the light cone modes are nonradiative. It is in the region outside the light cone that we can observe Dirac points for both sets of modes, appearing at the K and K' points as sketched in Fig. 3(c). Additionally, we also plot the band structure resulting from a quasistatic approximation, where we neglect the medium- and long-range terms in the Green's function and keep only the shortest-range one ($1/r^3$), but we still sum over all the lattice sites. This approximation is valid for very subwavelength arrays, such as the short-period quantum emitter arrays considered here, but since it does not include retardation it fails to predict the correct interactions with the light line for the most radiative modes, as can be seen in the figure. The fact that interactions among all the lattice elements are included results in the breaking of the chiral symmetry, which is characteristic of the honeycomb lattice in the nearest-neighbor limit and explains the lack of symmetry of the bands with respect to $\omega_{\mathbf{k}} = \omega_a$. While for this set of parameters the Dirac cones still appear close to $\omega_{\mathbf{k}} = \omega_a$, increasing lattice periodicity has a strong effect even in the dispersion of subradiant modes, as we discuss in Sec. VI.

IV. GENERALIZED DIRAC CONES IN THE OUT-OF-PLANE MODES OF ANISOTROPIC EMITTER ARRAYS

In this section we discuss the emergence and evolution of generalized Dirac cones for the out-of-plane modes of anisotropic dipolar arrays. The anisotropic lattices are shown in Figs. 2(b) and 2(c) for $\beta > 1$ and < 1 , respectively. As described above, the lattice vectors of the standard honeycomb, and hence the lattice periodicity, are kept, while the basis vector is changed from its honeycomb value, pushing together or apart the two sites in the unit cell. As we will see, the anisotropy of the interactions in the new lattices enables the emergence of generalized Dirac dispersions.

Figure 4 presents the evolution of the band structures for emitter arrays with the same lattice constant as in Fig. 3, fixed by $d_0 = 0.1\lambda_a$, as anisotropy changes from a value $\beta < 1$ [Figs. 4(a) and 4(b)], through $\beta = 1$ [Fig. 4(c)], to $\beta > 1$ [Fig. 4(d)]. In all panels, a sketch of the position of the generalized Dirac points in reciprocal space is shown in the left insets. The middle insets present line plots of the photonic dispersion along a vertical path in reciprocal space between two M points such that it passes through the K' , Γ , and K points. Additionally, the right insets display three-dimensional (3D) plots of the generalized cones.

We start with a critical value of anisotropy $\beta_c = 0.84$, for which the two out-of-plane modes cross in a semi-Dirac cone at the M point. As seen in Fig. 4(a), the dispersion is quadratic in the KMK' direction and linear in the orthogonal direction $\Gamma M\Gamma$. This kind of generalized Dirac dispersion has been shown to yield long-range anisotropic interactions with quantum emitters placed close to the metasurface [58].

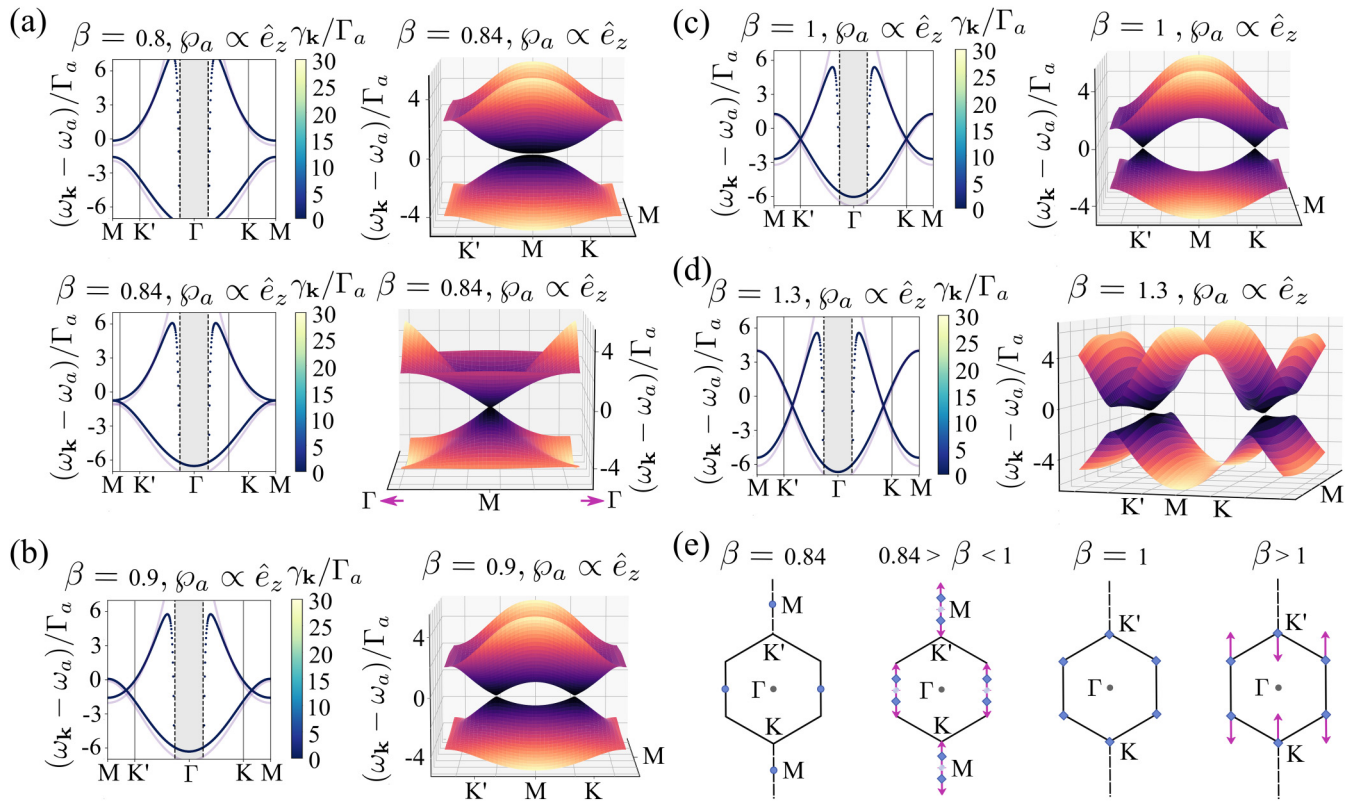


FIG. 4. Generalized Dirac cones in the out-of-plane modes of anisotropic honeycomb lattices. (a) Semi-Dirac cones emerge at the M points for a critical value of anisotropy $\beta_c = 0.84$. Dispersion is quadratic in the KMK' direction (shown in the line and right 3D plot), while it is linear in the orthogonal direction $\Gamma M\Gamma$ (see the left 3D plot). (b) As anisotropy decreases and the geometry of the honeycomb lattice is approached, $\beta_c < \beta < 1$, the semi-Dirac cones split into two Dirac cones that move away from M and towards K and K' . This is shown for $\beta = 0.9$. (c) When $\beta = 1$ the Dirac cones are at the K and K' points, as corresponds to a honeycomb lattice. (d) For $\beta > 1$, an anisotropic distribution of Dirac cones in reciprocal space develops. All Dirac points move vertically in the $K'\Gamma$ direction. In all cases the periodicity of the lattice is fixed by $d_0 = 0.1\lambda_a$. In the line plots, the quasistatic band structure is shown also for comparison as a light gray line. (e) Schematic representation of position and movement of the Dirac cones in reciprocal space which correspond, from left to right, to the configurations shown in (a)–(d), respectively.

Interestingly, these degeneracies have a zero topological charge [45]. Indeed, for higher anisotropy $\beta < \beta_c$ the bands are gapped, while for lower anisotropy $\beta > \beta_c$ the semi-Dirac cones split up into pairs of Dirac cones of opposite topological charge. That is, increasing β towards $\beta = 1$ splits up the semi-Dirac cones into pairs of Dirac cones that move in the vertical direction in k space towards the K and K' points. The pair of Dirac cones are shown in Fig. 4(b) for $\beta = 0.9$ and they display an anisotropic spatial distribution in reciprocal space, since they move in the vertical direction. Next the cones reach the K and K' points for $\beta = 1$, as corresponds to a honeycomb lattice, shown in Fig. 4(c). By increasing anisotropy again with $\beta > 1$, the Dirac cones continue moving vertically in reciprocal space past the K and K' points and towards the Γ point, as shown in Fig. 4(d) for $\beta = 1.3$. This results in a compression of the Dirac cones distribution in reciprocal space in the vertical direction (k_y) as well as in a flattening of the bands in the k_x direction. Hence, the cones are highly anisotropic, with a much lower slope in the k_x direction than in the k_y direction, as can be seen in the 3D plot in Fig. 4(d). As anisotropy is increased towards the maximum value ($\beta = 1.7321$), the anisotropy of the cones increases further with the slope in

the k_x direction away from the crossings approaching zero. Additionally, the position of the cones moves further, with the three top (and the three bottom) cones sketched in the figure tending to align with each other in the vertical direction.

As we have seen, anisotropy in the lattice enables unconventional Dirac dispersions. We now briefly comment on symmetry considerations behind this behavior. Introducing anisotropy in the lattice reduces the symmetry from C_{6v} to C_{2v} . Since the symmetry group does not have any irreducible representation of dimension greater than one, all degeneracies appearing in the anisotropic lattice are accidental. However, the topological nature of the Dirac cones, which poses non-trivial windings of opposite sign at the K and K' points, implies that they must be preserved when the lattice is adiabatically modified to introduce the anisotropy until they annihilate each other by merging at a semi-Dirac cone at the M point [45], as shown in Fig. 4. Furthermore, it should be noted that the specific geometry, that is, the value of lattice anisotropy parameter β for which the semi-Dirac cones appear, depends on the specific choice of periodicity, due to the long-range retarded interactions in the lattice, as is further discussed in Sec. VI.

V. GENERALIZED DIRAC CONES IN THE IN-PLANE MODES OF ANISOTROPIC LATTICES

After discussing the effect of lattice anisotropy on the dispersion of out-of-plane modes, we now consider the in-plane modes. First, we focus on the lowest two bands of the honeycomb metasurface [see Fig. 3(b)]. For these bands a semi-Dirac cone emerges at the M points for a critical value of anisotropy $\beta < 1$, which splits into two Dirac cones that move anisotropically in reciprocal space differently from the case discussed above for the out-of-plane modes.

The band structure for the in-plane modes of the metasurface is shown in Fig. 5(a) for a critical value of anisotropy $\beta_c = 0.587$. As for the out-of-plane modes, we see that these two bands touch with quadratic dispersion in one direction and linear in the orthogonal direction. However, differently from the case discussed above, in this case dispersion is quadratic in the horizontal direction ($\Gamma M \Gamma$ path, insets in the left column) and linear in the vertical direction ($K M K'$ path, insets in the right column). When moving away from this critical value of anisotropy by increasing β , each semi-Dirac cone splits into two Dirac cones that travel in reciprocal space. In contrast to the behavior of out-of-plane modes, in this case the Dirac cones travel towards Γ in the horizontal directions. This is shown in Figs. 5(b) and 5(c), as we now describe in detail.

Due to the retarded interactions characteristic of these subwavelength dipolar arrays, as β increases towards 1 and the cones travel towards Γ , they encounter the light line and the bands are strongly affected by interaction with it. This can be seen by comparing the full electrodynamic results (color coded) with the quasistatic approximation (light gray line) in the line plots in Figs. 5(b) and 5(c). In the quasistatic case, as β increases and the degeneracies move away from M , both bands retain their quadratic curvature in the horizontal direction but move in energy such that the quadratic touching point at M transforms into two isotropic type I Dirac points. On the other hand, when fully retarded interactions are taken into account, the top band presents a polaritonic-type splitting at the light line as it is prevented from entering the light cone and is instead strongly bent downward. This results in the Dirac crossings being tilted. Interestingly, the tilt emerges purely due to the radiative interactions between the emitters. Initially, the tilted cone is type I, as can be seen in the line and 3D plots in Fig. 5(b) for $\beta = 0.63$, but as β increases more the cone becomes more and more tilted, crossing the critical point where one of the bands is flat at the degeneracy (type III) and becoming type II, as shown for $\beta = 0.66$ in Fig. 5(c). This type of tilted Dirac cone arising due to strong polaritonic type interactions in subwavelength arrays was also observed in Ref. [44], where conventional subwavelength honeycomb lattices embedded inside a cavity were considered. While here it appears by modifying the lattice, in that work it requires the encapsulation of the array within two mirrors and tuning its distance. Finally, for a larger increase of β the degeneracy between the two bands is lost due to the strong interaction with the light line. In contrast, we note that in the quasistatic approximation the degeneracy is maintained until it reaches the Γ point for $\beta = 1$, as shown

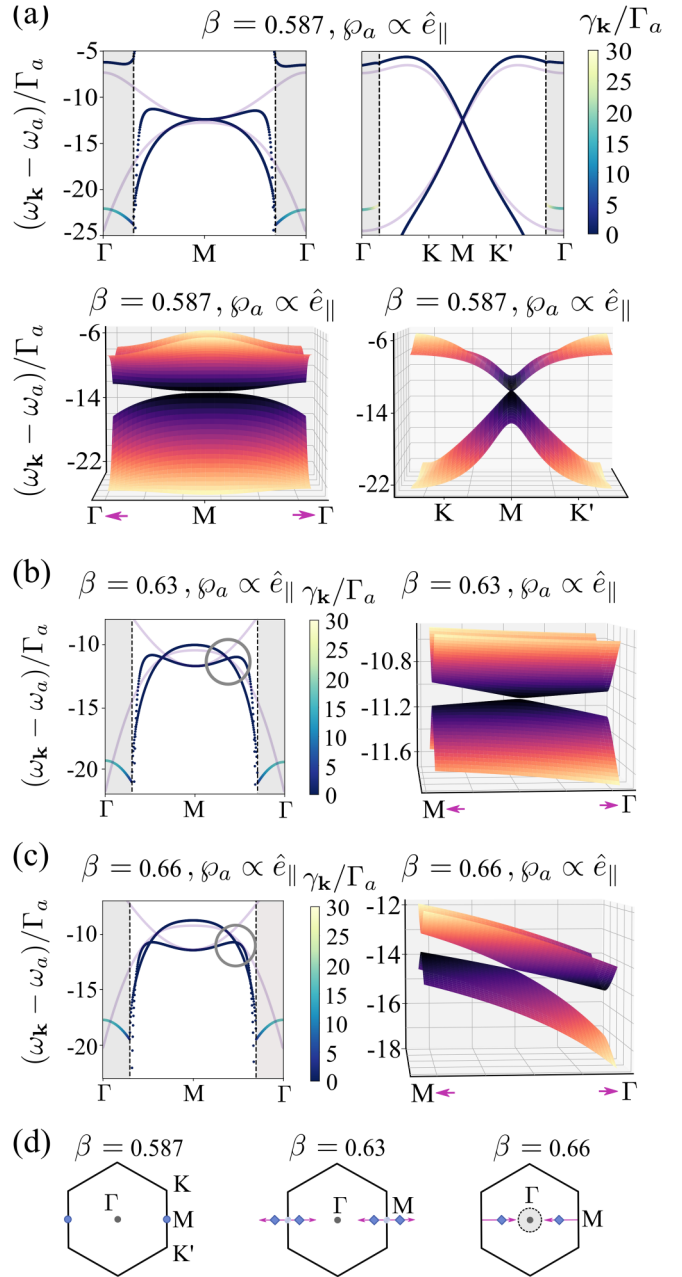


FIG. 5. Semi-Dirac and tilted Dirac cones for the in-plane modes of anisotropic honeycomb emitter arrays. (a) Semi-Dirac point formed by the crossing of the two lowest bands for a critical value of anisotropy $\beta = 0.587$. Dispersion in the $\Gamma M \Gamma$ and $K M K'$ directions is shown in the left and right line and 3D plots, respectively. (b) and (c) As anisotropy decreases, the semi-Dirac points split into two Dirac points that travel in the k_x direction towards Γ . At the same time, interactions with the light line tilt the cones. (b) For $\beta = 0.63$ the tilted cone is type I tilted, while (c) for $\beta = 0.66$ the cones are closer to the light line and become type II. The periodicity of the lattice is fixed as $d_0 = 0.1\lambda_a$. In the line plots, the quasistatic band structure is shown also for comparison as a light purple line. (d) Schematic representation of position and movement of the Dirac cones in reciprocal space which correspond, from left to right, to the configurations shown in (a)–(c), respectively.

for the honeycomb lattice in Fig. 3(b). This stresses the importance of including fully retarded interactions when studying subwavelength arrays.

Now we turn our attention to the two middle bands and study the emergence of generalized Dirac cones and their evolution from $\beta < 1$ to $\beta > 1$ in Fig. 6. First, for $\beta < 1$ we find Dirac cones along the ΓK and $\Gamma K'$ lines, traveling away from Γ and towards K and K' as β approaches 1. This is shown in Fig. 6(a). For a given value of anisotropy $\beta = 0.82$ (plots in insets in the top row), we find that the Dirac cones are tilted and of type II. For these parameters, they appear very close to the light line. However, and differently from the case discussed above or the work in Ref. [44], the type II tilt of these bands is not created by the interaction between the bands and the light line, since it is also present in the quasistatic bands, as can be seen in the light gray line in the plot. Next, as β increases, the cones move along vertical lines towards the K and K' points and the tilt transforms into a type I tilt, as shown for $\beta = 0.86$ (plots in insets in bottom row). Then, as expected, when $\beta = 1$ is reached, we observe conventional Dirac cones at the K and K' points in Fig. 6(b). Increasing anisotropy away from the honeycomb case with $\beta > 1$ results in a situation similar to that of the out-of-plane modes described above. As shown in Fig. 6(c), the Dirac cones move vertically in reciprocal space away from the K and K' points and as they do so they develop a strong anisotropy, with much flatter slopes along k_x than along k_y , as is clear from the 3D plot shown in Fig. 6(c).

VI. RETARDATION EFFECTS

Finally, in this section we further discuss the effect of retardation by considering lattices of increasing periodicity. We focus on the semi-Dirac cones that emerge for out-of-plane modes. Figures 7(a)–7(c) present band structures along a vertical path in reciprocal space between Γ and M for increasing values of $d_0/\lambda_a = 0.1, 0.15$, and 0.2 . We recall that d_0 gives the nearest-neighbor distance of the corresponding honeycomb lattice ($\beta = 1$) and it fixes the length of the lattice vectors as $|\mathbf{a}_{1,2}| = 2\sqrt{3}d_0 \approx 0.35\lambda_a, 0.52\lambda_a$, and $0.7\lambda_a$, respectively, for each case. First, in Fig. 7(a) we reproduce the quadratic dispersion featured by the semi-Dirac cone for $d_0/\lambda_a = 0.1$ and $\beta = 0.84$ discussed already in Fig. 4(a). In Fig. 7(b) we increase the lattice periodicity to $d_0/\lambda_a = 0.15$ and we see how the light cone moves further away from Γ , as expected. Additionally, the polariton-type interaction between the top band and the light line becomes stronger. However, there is still a semi-Dirac point for a larger value of anisotropy than in the previous case, $\beta = 0.8525$, with quadratic dispersion in the vertical direction as shown in Fig. 7(b) and linear dispersion in the orthogonal direction (not shown here). We stress that since the semi-Dirac points emerge at critical values of anisotropy and the bands depend on the lattice periodicity, the anisotropy value where the semi-Dirac cones emerge depends on the lattice periodicity. Finally, we increase the periodicity further to $d_0/\lambda_a = 0.2$ in Fig. 7(c), where retarded interactions become even more important and the bands are more strongly affected. For this case, we can

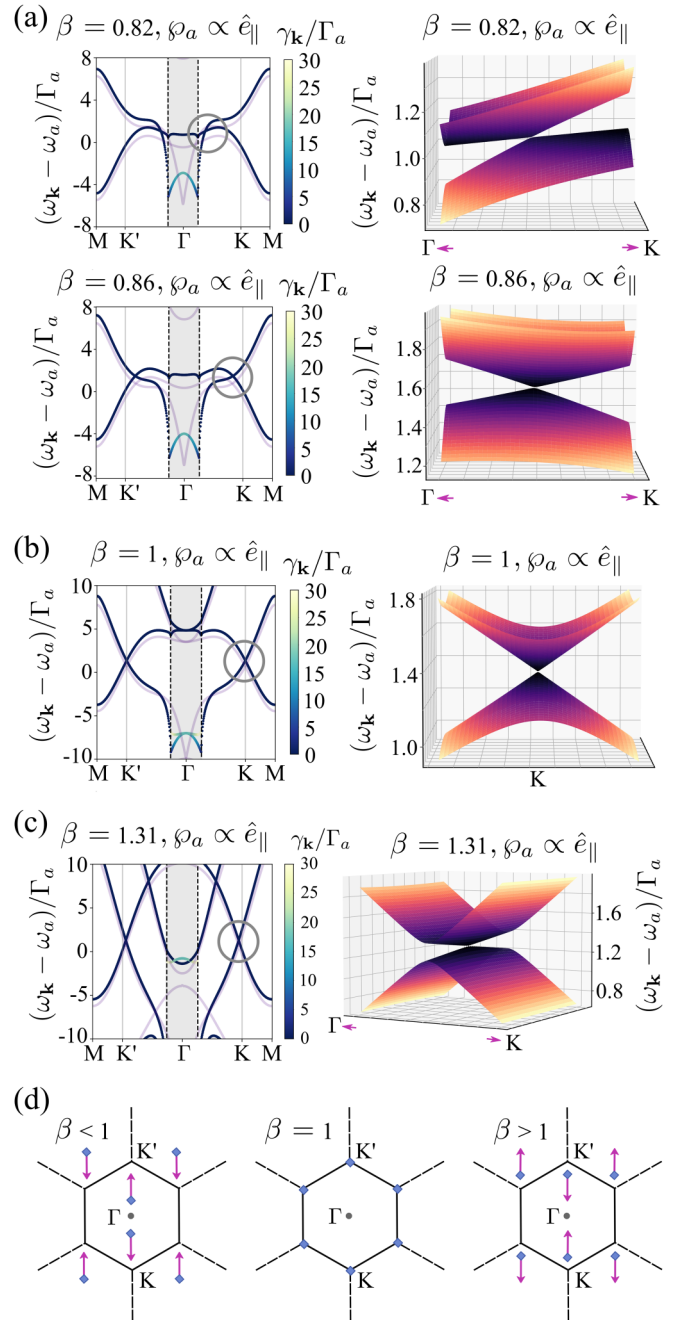


FIG. 6. Tilted Dirac cones and anisotropic distribution of Dirac cones in reciprocal space for the two middle in-plane modes of an anisotropic honeycomb metasurface. (a) Tilted Dirac cones appear in the ΓK lines for $\beta < 1$. For large anisotropy $\beta = 0.82$ (insets in the top row), the cones are type II. As β increases the cones transform into type I tilted cones as they approach the K' points ($\beta = 0.86$, insets in the bottom row). (b) For $\beta = 1$ isotropic Dirac cones at the K' points are found. (c) Cones move anisotropically in reciprocal space for $\beta > 1$ and the bands flatten in the horizontal direction. The periodicity of the lattice is fixed as $d_0 = 0.1\lambda_a$. In the line plots, the quasistatic band structure is shown also for comparison as a light purple line. (d) Schematic representation of position and movement of the Dirac cones in reciprocal space which correspond, from left to right, to the configurations shown in (a)–(c), respectively.

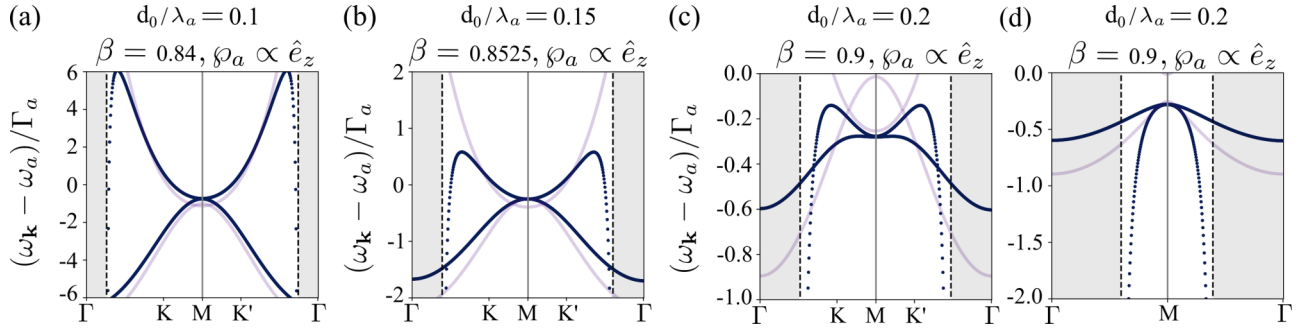


FIG. 7. Retardation effects are visible for increasing lattice periodicity. Band structures of out-of-plane modes are shown in the vertical direction in reciprocal space for (a) $d_0/\lambda_a = 0.1$ and $\beta = 0.84$, (b) $d_0/\lambda_a = 0.15$ and $\beta = 0.8525$, and (c) and (d) $d_0/\lambda_a = 0.2$ and $\beta = 0.9$, along the ΓKM and ΓM paths. In (a) and (b) the degeneracy is a semi-Dirac cone (the linear dispersion in the orthogonal direction is not shown here). In (c) and (d) the semi-Dirac cone is lost as dispersion is quadratic in both directions due to strong interactions with the light line.

still find a quadratic touching point for $\beta = 0.9$. However, the linear crossing in the orthogonal direction is lost due to the strong modification of the bands owing to retardation, and the degeneracy is quadratic also in this direction [see Fig. 7(d)]. Interestingly, the modification of the bands leads to an anisotropic quadratic degeneracy, as the curvature of the top band flips sign between orthogonal directions. These results show that the behavior of the generalized Dirac cones discussed in this work are robust as long as the periodicity is kept small, but may change when the periodicity of the arrays is not very subwavelength $|\mathbf{a}_{1,2}| \gtrsim 0.7\lambda_a$. Additionally, they show that accounting for fully retarded interactions in quantum metasurfaces is important, as their behavior may strongly deviate from what a quasistatic approximation would predict, even giving rise to different effects such as the tilted Dirac cones discussed above.

VII. CONCLUSION

We discussed the presence and manipulation of generalized Dirac dispersions in a honeycomb emitter array of subwavelength periodicity. We first reviewed the properties of Dirac cones and then showed how modified dispersions emerge by introducing uniaxial anisotropy to the lattice, that is, by moving the two emitters in the unit cell farther away or closer together in a given direction. Specifically, we observed semi-Dirac points, which possess linear and quadratic dispersion in orthogonal directions, and tilted Dirac cones that change the local density of states at the degeneracy point from vanishing (type I) to diverging (types II and III). We explained the emergence and discussed the manipulation of each type of dispersion relation in the subradiant out-of-plane and in-

plane modes, as well as their movement in reciprocal space with the anisotropy of the lattice. Moreover, we included a detailed discussion of the importance of including retardation effects to describe the system and how they can affect the Dirac dispersions. Our results show that the behavior of the generalized Dirac cones is robust to retardation effects and that accounting for retarded interactions beyond quasistatic ones in the modeling of subwavelength emitter arrays is important in order to predict the correct behavior of the modes. Importantly, tilted Dirac cones in this system are a result of the dipole-dipole electromagnetic coupling between the elements in the array, which is of long-range and retarded nature. The engineering and manipulation of such energy dispersions can modify substantially the quantum dynamics of local probes placed near the metasurface giving rise to exotic forms of light-matter interactions.

ACKNOWLEDGMENTS

M.B.d.P. acknowledges support from the Spanish Ministerio de Ciencia e Innovación (Grant No. PID2019-109905GA-C2) and from Eusko Jaurlaritza (Grant No. KK-2021/00082). A.G.-T. acknowledges support from CSIC Research Platform on Quantum Technologies PTI-001, from Spanish Project No. PGC2018-094792-B-100 (MCIU/AEI/FEDER, EU), and from the Proyecto Sinérgico CAM Y2020/TCS-6545 (NanoQuCo-CM). P.A.H. acknowledges funding from Fundação para a Ciência e a Tecnologia and Instituto de Telecomunicações under Projects No. UIDB/50008/2020 and No. UTAPEXPL/NPN/0022/2021 and the CEEC Individual Program No. CEECIND/02947/2020.

- [1] D. R. Smith, J. B. Pendry, and M. C. K. Wiltshire, *Science* **305**, 788 (2004).
- [2] N. Yu and F. Capasso, *Nat. Mater.* **13**, 139 (2014).
- [3] N. Meinzer, W. L. Barnes, and I. R. Hooper, *Nat. Photon.* **8**, 889 (2014).
- [4] V. G. Kravets, A. V. Kabashin, W. L. Barnes, and A. N. Grigorenko, *Chem. Rev.* **118**, 5912 (2018).
- [5] W. Wang, M. Ramezani, A. I. Väkeväinen, P. Törmä, J. G. Rivas, and T. W. Odom, *Mater. Today* **21**, 303 (2018).
- [6] A. Poddubny, A. Miroshnichenko, A. Slobozhanyuk, and Y. Kivshar, *ACS Photon.* **1**, 101 (2014).
- [7] S. Yves, R. Fleury, T. Berthelot, M. Fink, F. Lemoult, and G. Lerosey, *Nat. Commun.* **8**, 16023 (2017).
- [8] S. R. Poochok, X. Xiao, P. A. Huidobro, and V. Giannini, *ACS Photon.* **5**, 2271 (2018).
- [9] C. A. Downing, T. J. Sturges, G. Weick, M. Stobińska, and L. Martín-Moreno, *Phys. Rev. Lett.* **123**, 217401 (2019).

- [10] M. Proctor, R. V. Craster, S. A. Maier, V. Giannini, and P. A. Huidobro, *ACS Photon.* **6**, 2985 (2019).
- [11] C. A. Downing and L. Martín-Moreno, *Nanophotonics* **10**, 513 (2021).
- [12] C.-R. Mann, S. A. R. Horsley, and E. Mariani, *Nat. Photon.* **14**, 669 (2020).
- [13] M. Zhou, J. Liu, M. A. Kats, and Z. Yu, *ACS Photon.* **4**, 1279 (2017).
- [14] R. Bekenstein, I. Pikovski, H. Pichler, E. Shahmoon, S. F. Yelin, and M. D. Lukin, *Nat. Phys.* **16**, 676 (2020).
- [15] A. S. Solntsev, G. S. Agarwal, and Y. Y. Kivshar, *Nat. Photon.* **15**, 327 (2021).
- [16] G. Zumofen, N. M. Mojarad, V. Sandoghdar, and M. Agio, *Phys. Rev. Lett.* **101**, 180404 (2008).
- [17] I. Bloch, *Nat. Phys.* **1**, 23 (2005).
- [18] S. D. Jenkins and J. Ruostekoski, *Phys. Rev. A* **86**, 031602(R) (2012).
- [19] B. Olmos, D. Yu, Y. Singh, F. Schreck, K. Bongs, and I. Lesanovsky, *Phys. Rev. Lett.* **110**, 143602 (2013).
- [20] R. J. Bettles, S. A. Gardiner, and C. S. Adams, *Phys. Rev. Lett.* **116**, 103602 (2016).
- [21] N. J. Schilder, C. Sauvan, J.-P. Hugonin, S. Jennewein, Y. R. P. Sortais, A. Browaeys, and J.-J. Greffet, *Phys. Rev. A* **93**, 063835 (2016).
- [22] J. Ruostekoski and J. Javanainen, *Phys. Rev. Lett.* **117**, 143602 (2016).
- [23] E. Shahmoon, D. S. Wild, M. D. Lukin, and S. F. Yelin, *Phys. Rev. Lett.* **118**, 113601 (2017).
- [24] A. Asenjo-Garcia, M. Moreno-Cardoner, A. Albrecht, H. J. Kimble, and D. E. Chang, *Phys. Rev. X* **7**, 031024 (2017).
- [25] S. J. Masson and A. Asenjo-Garcia, *Phys. Rev. Research* **2**, 043213 (2020).
- [26] T. L. Patti, D. S. Wild, E. Shahmoon, M. D. Lukin, and S. F. Yelin, *Phys. Rev. Lett.* **126**, 223602 (2021).
- [27] K. Brechtelsbauer and D. Malz, *Phys. Rev. A* **104**, 013701 (2021).
- [28] D. Castells-Graells, D. Malz, C. C. Rusconi, and J. I. Cirac, *Phys. Rev. A* **104**, 063707 (2021).
- [29] D. Fernández-Fernández and A. González-Tudela, *Phys. Rev. Lett.* **128**, 113601 (2022).
- [30] J. Perczel, J. Borregaard, D. E. Chang, H. Pichler, S. F. Yelin, P. Zoller, and M. D. Lukin, *Phys. Rev. Lett.* **119**, 023603 (2017).
- [31] R. J. Bettles, Minaji, C. S. Adams, I. Lesanovsky, and B. Olmos, *Phys. Rev. A* **96**, 041603(R) (2017).
- [32] R. Alaei, B. Gurlek, M. Albooyeh, D. Martín-Cano, and V. Sandoghdar, *Phys. Rev. Lett.* **125**, 063601 (2020).
- [33] K. E. Ballantine and J. Ruostekoski, *Phys. Rev. Lett.* **125**, 143604 (2020).
- [34] J. Rui, D. Wei, A. Rubio-Abadal, S. Hollerith, J. Zeiher, D. M. Stamper-Kurn, C. Gross, and I. Bloch, *Nature (London)* **583**, 369 (2020).
- [35] D. E. Chang, J. S. Douglas, A. González-Tudela, C.-L. Hung, and H. Kimble, *Rev. Mod. Phys.* **90**, 031002 (2018).
- [36] A. H. Castro Neto, F. Guinea, N. M. R. Peres, K. S. Novoselov, and A. K. Geim, *Rev. Mod. Phys.* **81**, 109 (2009).
- [37] F. D. M. Haldane and S. Raghu, *Phys. Rev. Lett.* **100**, 013904 (2008).
- [38] R. A. Sepkhanov, Y. B. Bazaliy, and C. W. J. Beenakker, *Phys. Rev. A* **75**, 063813 (2007).
- [39] S. R. Zandbergen and M. J. A. de Dood, *Phys. Rev. Lett.* **104**, 043903 (2010).
- [40] X. Huang, Y. Lai, Z. H. Hang, H. Zheng, and C. T. Chan, *Nat. Mater.* **10**, 582 (2011).
- [41] J. Bravo-Abad, J. D. Joannopoulos, and M. Soljačić, *Proc. Natl. Acad. Sci. USA* **109**, 9761 (2012).
- [42] B. Yang, Q. Guo, B. Tremain, R. Liu, L. E. Barr, Q. Yan, W. Gao, H. Liu, Y. Xiang, J. Chen, C. Fang, A. Hibbins, L. Lu, and S. Zhang, *Science* **359**, 1013 (2018).
- [43] C. Hu, Z. Li, R. Tong, X. Wu, Z. Xia, L. Wang, S. Li, Y. Huang, S. Wang, B. Hou, C. T. Chan, and W. Wen, *Phys. Rev. Lett.* **121**, 024301 (2018).
- [44] C.-R. Mann, T. J. Sturges, G. Weick, W. L. Barnes, and E. Mariani, *Nat. Commun.* **9**, 2194 (2018).
- [45] M. Milićević, G. Montambaux, T. Ozawa, O. Jamadi, B. Real, I. Sagnes, A. Lemaître, L. Le Gratiet, A. Harouri, J. Bloch, and A. Amo, *Phys. Rev. X* **9**, 031010 (2019).
- [46] B. Real, O. Jamadi, M. Milićević, N. Pernet, P. St-Jean, T. Ozawa, G. Montambaux, I. Sagnes, A. Lemaître, L. Le Gratiet, A. Harouri, S. Ravets, J. Bloch, and A. Amo, *Phys. Rev. Lett.* **125**, 186601 (2020).
- [47] J. Kim, S. Yu, and N. Park, *Phys. Rev. Appl.* **13**, 044015 (2020).
- [48] G. Montambaux, F. Piéchon, J.-N. Fuchs, and M. O. Goerbig, *Phys. Rev. B* **80**, 153412 (2009).
- [49] L. Tarruell, D. Greif, T. Uehlinger, G. Jotzu, and T. Esslinger, *Nature (London)* **483**, 302 (2012).
- [50] M. Bellec, U. Kuhl, G. Montambaux, and F. Mortessagne, *Phys. Rev. Lett.* **110**, 033902 (2013).
- [51] M. O. Goerbig, J.-N. Fuchs, G. Montambaux, and F. Piéchon, *Phys. Rev. B* **78**, 045415 (2008).
- [52] Y. Hasegawa, R. Konno, H. Nakano, and M. Kohmoto, *Phys. Rev. B* **74**, 033413 (2006).
- [53] P. Dietl, F. Piéchon, and G. Montambaux, *Phys. Rev. Lett.* **100**, 236405 (2008).
- [54] A. González-Tudela and J. I. Cirac, *Phys. Rev. A* **97**, 043831 (2018).
- [55] J. Perczel and M. D. Lukin, *Phys. Rev. A* **101**, 033822 (2020).
- [56] E. P. Navarro-Barón, H. Vinck-Posada, and A. González-Tudela, *ACS Photon.* **8**, 3209 (2021).
- [57] J. Perczel, J. Borregaard, D. E. Chang, S. F. Yelin, and M. D. Lukin, *Phys. Rev. Lett.* **124**, 083603 (2020).
- [58] J. Redondo-Yuste, M. B. de Paz, P. A. Huidobro, and A. González-Tudela, *New J. Phys.* **23**, 103018 (2021).
- [59] J. Perczel, J. Borregaard, D. E. Chang, H. Pichler, S. F. Yelin, P. Zoller, and M. D. Lukin, *Phys. Rev. A* **96**, 063801 (2017).
- [60] R. H. Lehberg, *Phys. Rev. A* **2**, 883 (1970).
- [61] R. H. Lehberg, *Phys. Rev. A* **2**, 889 (1970).
- [62] P. P. Ewald, *Ann. Phys. (Leipzig)* **369**, 253 (1921).
- [63] C. M. Linton, *SIAM Rev.* **52**, 630 (2010).